

Oxygen Evolution Activity of Amorphous Cobalt Oxyhydroxides: Interconnecting Precatalyst Reconstruction, Long-Range Order, Buffer-Binding, Morphology, Mass Transport, and Operation Temperature

J. Niklas Hausmann, Stefan Mebs, Holger Dau,* Matthias Driess,* and Prashanth W. Menezes*

Nanocrystalline or amorphous cobalt oxyhydroxides (CoCat) are promising electrocatalysts for the oxygen evolution reaction (OER). While having the same short-range order, CoCat phases possess different electrocatalytic properties. This phenomenon is not conclusively understood, as multiple interdependent parameters affect the OER activity simultaneously. Herein, a layered cobalt borophosphate precatalyst, $\text{Co}(\text{H}_2\text{O})_2[\text{B}_2\text{P}_2\text{O}_8(\text{OH})_2]\cdot\text{H}_2\text{O}$, is fully reconstructed into two different CoCat phases. In contrast to previous reports, this reconstruction is not initiated at the surface but at the electrode substrate to catalyst interface. Ex situ and in situ investigations of the two borophosphate derived CoCats, as well as the prominent CoP_i and CoB_i , identify differences in the Tafel slope/range, buffer binding and content, long-range order, number of accessible edge sites, redox activity, and morphology. Considering and interconnecting these aspects together with proton mass-transport limitations, a comprehensive picture is provided explaining the different OER activities. The most decisive factors are the buffers used for reconstruction, the number of edge sites that are not inhibited by irreversibly bonded buffers, and the morphology. With this acquired knowledge, an optimized OER system is realized operating in near-neutral potassium borate medium at $1.62 \pm 0.03 \text{ V}_{\text{RHE}}$ yielding 250 mA cm^{-2} at 65°C for 1 month without degrading performance.

several advantages (e.g., direct coupling to corrosion sensitive photoabsorbers^[2] and ideal operation with cathodic carbon dioxide reduction^[1,3]). However, the efficiency in near-neutral pH is low compared to systems operating under strongly acidic or alkaline conditions due to slow OER kinetics and insufficient mass transport.^[4,5]

In near-neutral media, the most prominent OER catalyst is CoP_i , an amorphous, phosphate containing cobalt oxide comprising edge sharing $[\text{CoO}_6]$ octahedra forming layers (domains, **Figure 1** left) of molecular size ($\approx 11\text{--}14 \text{ \AA}$).^[6–8] These domains arrange in an unordered way (**Figure 1** right) with ions and water in the interlayer space resulting in an electrolyte penetrable structure. CoP_i is obtained by anodic electrodeposition from aqueous Co^{2+} solutions in potassium phosphate (KP_i) buffer. Also, other buffers have been used such as potassium borate (KB_i) resulting in larger domain sizes ($20\text{--}35 \text{ \AA}$) and a more ordered stacking (CoB_i).^[6–9]

CoP_i and CoB_i are bulk-active OER catalysts.^[6,8,10,11] However, the turnover frequency per loaded cobalt (TOF_{Co}) is a function of the catalyst loading and current density, indicating mass or charge-transport limitations.^[6,8,10,11] The decline of the TOF_{Co} is significantly more pronounced in CoP_i proving that these


1. Introduction

The oxygen evolution reaction (OER) is key to supply electrons and protons for the electrocatalytic formation of sustainable fuels.^[1] The performance of it in near-neutral media has

J. N. Hausmann, M. Driess, P. W. Menezes
Department of Chemistry: Metalorganics and Inorganic Materials
Technical University of Berlin
Straße des 17 Juni 135, Sekr. C2, 10623 Berlin, Germany
E-mail: matthias.driess@tu-berlin.de;
prashanth.menezes@mailbox.tu-berlin.de

S. Mebs, H. Dau
Department of Physics
Free University of Berlin
Arnimallee 14, 14195 Berlin, Germany
E-mail: holger.dau@fu-berlin.de

P. W. Menezes
Material Chemistry Group for Thin Film Catalysis—CatLab
Helmholtz-Center Berlin for Materials and Energy
Albert-Einstein-Str. 15, 12489 Berlin, Germany

 The ORCID identification number(s) for the author(s) of this article can be found under <https://doi.org/10.1002/adma.202207494>.

© 2022 The Authors. Advanced Materials published by Wiley-VCH GmbH. This is an open access article under the terms of the Creative Commons Attribution License, which permits use, distribution and reproduction in any medium, provided the original work is properly cited.

DOI: 10.1002/adma.202207494

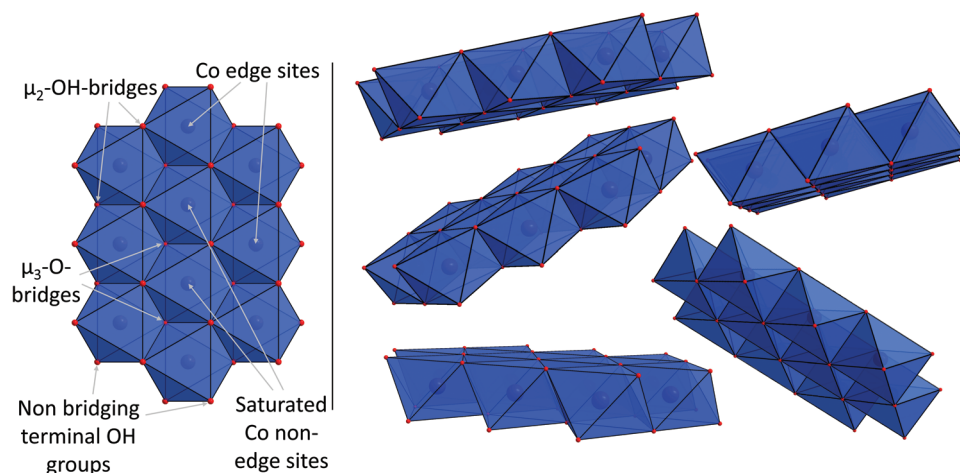


Figure 1. Description of the amorphous CoCat structure comprising cobalt (blue spheres) coordinated octahedrally by oxygen atoms (red spheres). These $[\text{CoO}_6]$ octahedra (blue) are connected through edge sharing resulting in molecular domains (left) that are arranged in an unordered way (right), with water molecules and ions (not shown here) filling the interdomain voids.

limitations are catalyst dependent.^[6,11] Furthermore, it has been shown that near-surface cobalt has a higher TOF_{Co} .^[10] Until now, the reasons for the activity differences are unknown, but recent quasi in situ conductivity measurements revealed that electron conductivity can be excluded.^[12]

Since the discovery of CoP_i , many cobalt-based electrode materials for the OER in (near)neutral media have been reported.^[13–22] These materials act as precatalysts and reconstruct into amorphous CoO_xH_y phases (called CoCat) with structures similar to the ones of CoP_i and CoB_i .^[10,15–18,21,23,24] The significant differences in the OER performances of CoP_i , CoB_i , and other amorphous CoO_xH_y catalysts show that various CoCat phases with distinct electrochemical properties exist. The difference between CoP_i and CoB_i is caused by the buffer in which they are deposited. However, little is known on the effect of different buffers on the CoCat phase formed from a precatalyst especially as previously studied systems with various buffers did not fully convert to CoCat.^[24,25] Furthermore, it is unknown how far the nature of precursor material influences which kind of CoCat is formed and how structural and morphological changes of CoCat phases influence the OER activity.

In this regard, herein, we want to address the following research questions:

1. Do the precatalyst nature and the buffer type used for the reconstruction influence the properties of the finally formed CoCat catalyst?
2. How can the activity difference of various CoCat phases be explained on a molecular level and how can the OER properties of these phases be optimized?
3. What causes the different magnitudes of mass-transport limitations of various CoCat phases and how can they be minimized?
4. Can noble-metal-free OER electrodes be realized that, in near-neutral medium, can achieve high current densities at overpotentials in the range of those in strongly acidic or alkaline media?

To answer these research questions, we synthesized a set of four different OER catalysts that all contain a CoCat like structure

but have different electrocatalytic properties. Two of these catalysts are the previously reported CoP_i and CoB_i . The other two catalysts were obtained by the reconstruction of a layered cobalt borophosphate model precatalyst, $\text{Co}(\text{H}_2\text{O})_2[\text{B}_2\text{P}_2\text{O}_8(\text{OH})_2] \cdot \text{H}_2\text{O}$ (called CoBP, for a structure description see Figure S1, Supporting Information), in borate or phosphate buffer. CoBP is ideal for this purpose, as it contains equal quantities of borate and phosphate in its structure and previously borophosphate derived catalysts showed excellent OER properties.^[26–28] The aim of this manuscript is especially to interconnect different phenomena affecting the OER performance to develop a model consistent with previous reports and able to explain the activity differences and mass-transport limitations of the four CoCat phases and two cobalt oxides (CoO and Co_3O_4). In this regard, the precatalyst reconstruction conditions, long-range order, buffer-binding, and morphology are considered.

Herein, we find that, during the OER, CoBP can be fully reconstructed into two different CoCat phases with distinct catalytic properties depending on the buffer (KP_i and KB_i). Comparing these two catalysts with CoP_i and CoB_i shows that all catalysts have the same short-range order. Nevertheless, significant differences in the catalytic activity, Tafel slope, linear Tafel range, the buffer-binding and content, the degree of order/domain size, the number of available edge sites, and the morphology were observed. With this data set, we succeed in connecting the different electrocatalytic properties to variations in chemical structure and morphology of the four catalysts. Following these new insights, we designed a system that can perform the OER in near-neutral media at 1.63 V_{RHE} achieving a current density of 250 mA cm^{-2} for 1 month without activity degradation.

2. Results and Discussion

2.1. Characterization of As-Prepared $\text{Co}(\text{H}_2\text{O})_2[\text{B}_2\text{P}_2\text{O}_8(\text{OH})_2] \cdot \text{H}_2\text{O}$

CoBP was obtained through hydrothermal synthesis^[29] and characterized by powder X-ray diffraction (pXRD, Figure S2,

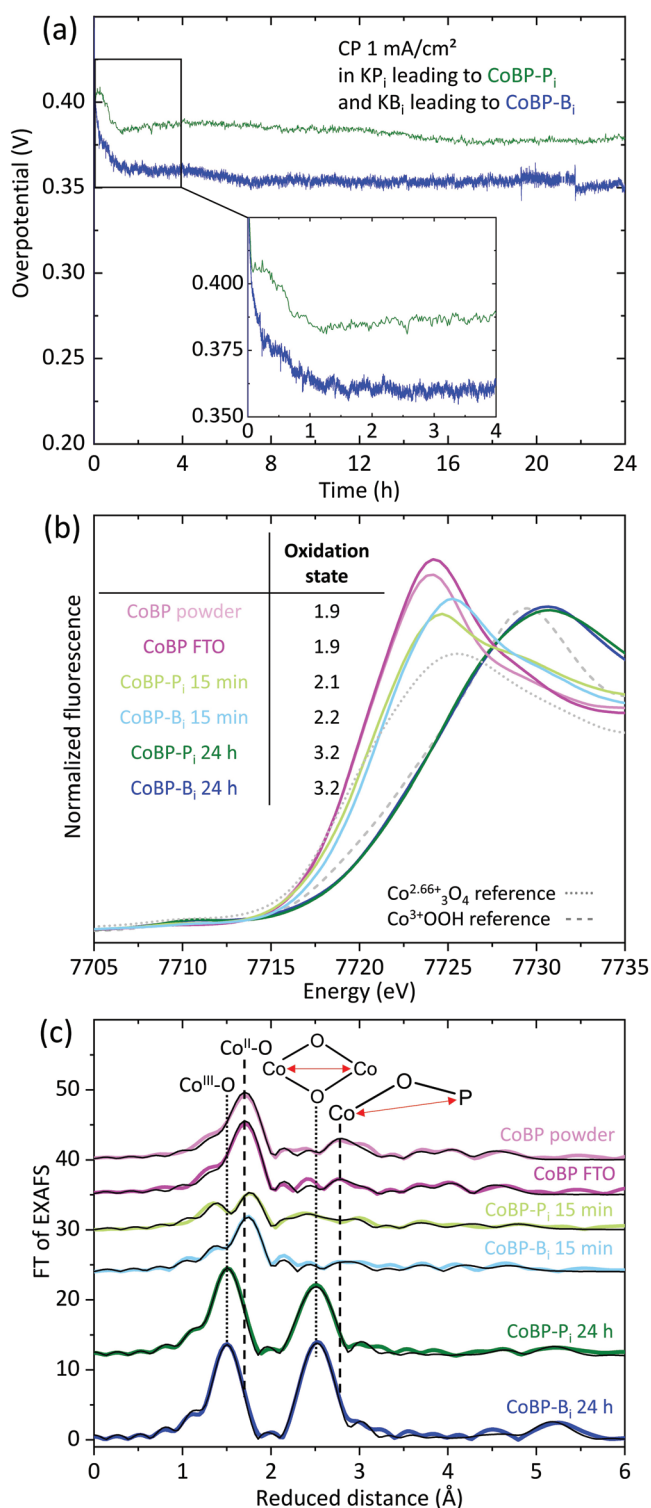


Figure 2. The reconstruction of $\text{Co}(\text{H}_2\text{O})_2[\text{B}_2\text{P}_2\text{O}_8(\text{OH})_2]\cdot\text{H}_2\text{O}$ (CoBP) in stirred 0.1 M KP_i and KB_i buffer during OER. a) The *iR*-corrected CP (1 mA cm⁻²) data of CoBP in 0.1 M KP_i (pH 7.20) or KB_i (pH 9.24). The samples obtained at the end of this 24 h measurements are called CoBP-P_i and CoBP-B_i depending on the buffer (see also Figure 6a). b) Co K-edge XANES data of various CoBP samples before measurement and quasi in situ (all samples were freeze-quenched at $\eta = 400$ mV) after 15 min or 24 h CP at 1 mA cm⁻². Figure S10, Supporting Information, shows the

Supporting Information), inductively coupled plasma optical emission spectroscopy (ICP-OES, Figure S2 inset, Supporting Information), scanning electron microscopy (SEM) with energy-dispersive X-ray (EDX) mapping (Figures S3 and S4, Supporting Information), transmission electron microscopy (TEM) with selected-area electron diffraction (SAED, Figure S5, Supporting Information), X-ray photoelectron spectroscopy (XPS; Figure S6, Supporting Information), and X-ray absorption spectroscopy including extended X-ray absorption fine structure (EXAFS; Figure 2c), and X-ray absorption near edge structure (XANES; Figure 2b) analyses. All methods confirm the formation of a pristine CoBP phase.

2.2. The Reconstruction of CoBP in KP_i and KB_i

To investigate the electrochemical properties of CoBP, we electrophoretically deposited it on FTO without any binder (for SEM/EDX see Figures S7 and S8, Supporting Information, and for XAS Figure 2b,c). With the obtained electrode, we conducted chronopotentiometry (CP) experiments at 1 mA cm⁻² for 24 h in 0.1 M KP_i (pH = 7.20) and 0.1 M KB_i (pH = 9.24) buffer (Figure 2a). The samples of CoBP after 24 h CP in KP_i or KB_i are called CoBP-P_i and CoBP-B_i, respectively. In the first 1.5 h of the CP experiment, the potential is decreasing in a similar way for both buffers. After that, it remains constant. The overpotentials at 1 mA cm⁻² (η_1) of CoBP-P_i and CoBP-B_i are 379 ± 7 and 352 ± 7 mV.

After 24 h of CP, the initially highly crystalline CoBP phase is X-ray amorphous (Figure S9, Supporting Information). Furthermore, ICP-OES shows that CoBP-P_i contains no boron anymore and CoBP-B_i has no phosphorous (inset Figure S9, Supporting Information). Thus, the initially crystalline CoBP phase reconstructed/transformed completely.

2.2.1. Quasi In Situ XAS

To understand this reconstruction, we performed XAS on samples freeze-quenched at $\eta = 400$ mV after 15 min and 24 h CP at 1 mA cm⁻² (denoted as quasi in situ, see Characterization Details in Supporting Information for more information).^[30] The XANES spectra reveal that in both buffers, the cobalt bulk oxidation state increases over time and is 3.2 after 24 h (Figure 2b, for oxidation state determination see Figure S10, Supporting Information). This oxidation state is consistent with quasi in situ measurements on CoP_i and indicates that the CoBP phase fully reconstructed into a CoCat phase during operation.^[23,30] After 15 min, the oxidation state is around 2.1–2.2 revealing an incomplete reconstruction. All EXAFS spectra could be simulated by a combination of the initial CoBP phase

linear regression used to determine the oxidation states. c) Co K-edge EXAFS plots of the same samples like in (b). The two most important distances of the as-prepared CoBP (Co^{II}-O and Co-P, dashed lines) and the quasi in situ formed CoCat phase (Co^{III}-O and Co^{III}-(O)-Co^{III}, dotted lines) are depicted. The black lines show the simulation. EXAFS simulation parameters and experimental data in *k*-space are provided in Tables S2 and S5 and Figure S11, Supporting Information.

and a CoCat model (Figure 2c and Figure S11 and Tables S2, S5, and S6, Supporting Information). The initial CoBP phase has two characteristic $\text{Co}^{\text{II}}\text{-O}$ and $\text{Co}^{\text{II}}\text{(O)-P}$ EXAFS peaks (dashed lines in Figure 2c) that are distinguishable from the most pronounced $\text{Co}^{\text{III}}\text{-O}$ and $\text{Co}^{\text{III}}\text{(O)-Co}^{\text{III}}$ peaks of CoCat (dotted lines in Figure 2c). After 15 min, the $\text{Co}^{\text{II}}\text{-O}$ and $\text{Co}^{\text{II}}\text{(O)-P}$ signal intensity decreased significantly already. For both buffers, EXAFS simulations of these spectra reveal a ratio of $\text{Co}^{\text{II}}\text{-O}$ to $\text{Co}^{\text{III}}\text{-O}$ of three to one indicating that around 25% of the CoBP material has converted into a CoCat related phase. After 24 h, the EXAFS spectra of both materials are consistent with a complete reconstruction into CoCat. A detailed discussion of this data can be found in Section 2.4.3.

2.2.2. XPS and Electron Microscopy

Additionally, ex situ XPS measurements were conducted after 15 min and 24 h of CP (Figures S12–S15, Supporting Information). After 24 h for both CoBP- P_i and - B_i , the Co 2p XPS reveals a mixed surface oxidation state of Co^{II} and Co^{III} . Such a reduced surface oxidation state compared to the bulk (bulk oxidation state is around three, see Section 2.4.3) is consistent with previous reports on CoCat.^[31,32] The P 2p, B 1s, and O 1s spectra confirm the formation of a CoCat phase with either almost only a phosphate (CoBP- P_i) or only borate (CoBP- B_i) surface species. Surprisingly, the XPS measurements after 15 min show that the outer electrode surface did not reconstruct at all. This observation is remarkable, as such reconstructions are widely reported to start at the surface of the particles leading to the formation

of core–shell structures, in which the core is the precatalyst and the shell an quasi in situ formed oxidic phase in contact with the electrolyte.

To localize the CoCat phase formed after 15 min, which was identified by XAS, SEM-EDX measurements from the electrode cross section were performed together with visible-light images from the front and reverse sides of the transparent electrode (Figure 3 and Figure S16, Supporting Information). This data reveals that the reconstruction starts near the conducting FTO electrode substrate and from there it proceeds to the top layers of the film. Thus, after 15 min, the newly formed CoCat phase is still covered with crystalline CoBP explaining the XPS results. A reason for this unprecedented kind of reconstruction is that CoBP is an insulator and that an anodic potential is a prerequisite for the reconstruction. Therefore, initially, only the material in direct contact with the conducting FTO is electronically wired to the anode. Thus, the reconstruction begins there and can then proceed at the interface of the crystalline CoBP with the newly formed, electron conducting CoCat to the outer CoBP particles of the film.

It is crucial to consider this manner of reconstruction when post catalytic characterizations on OER (pre)catalysts are performed, as the XPS, pXRD, and electron microscopic data after and before catalysis might be indistinguishable, because the reconstructed phase is hidden under the intact precatalysts. Thus, potentially leading to the false conclusion that a precatalyst does not reconstruct.

Additional to the SEM cross section investigation, further electron microscopic investigations have been performed. The SEM/EDX mappings show a homogeneous distribution of the

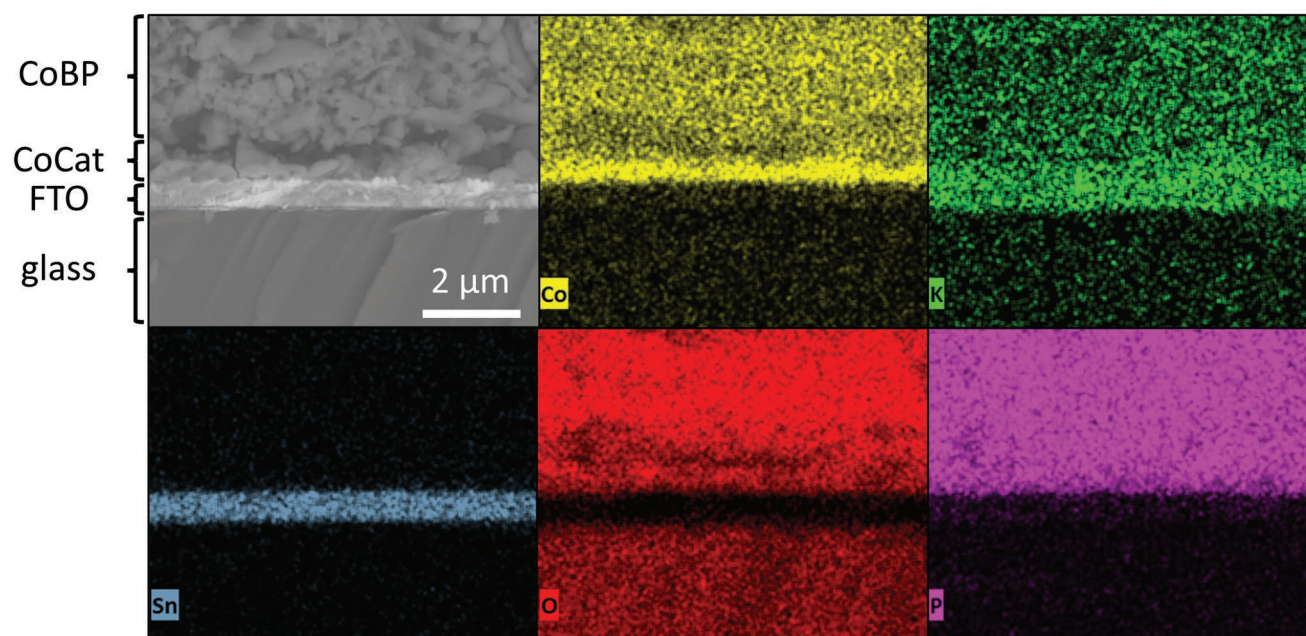


Figure 3. Cross-sectional SEM/EDX mapping of $\text{Co}(\text{H}_2\text{O})_2[\text{B}_2\text{P}_2\text{O}_8(\text{OH})_2]\cdot\text{H}_2\text{O}$ (CoBP) on an FTO glass plate after 15 min OER CP (1 ma cm^{-2}) in 0.1 M KP_i buffer. CoCat contains more cobalt and potassium and less oxygen than CoBP. The potassium and tin EDX peaks overlap which explains why the FTO is marked in green in the mapping. A deconvoluted EDX spectrum of the FTO shows that no substantial amount of potassium is present. This spectrum also contains an oxygen peak. Nevertheless, it is less intense than the one of the CoBP and CoCat phases, leading to the weak red color in the oxygen mapping for FTO. Overall, the mappings reveal, supported by the data of Figures S12 and S16, Supporting Information, that the reconstruction of CoBP to CoCat did not start at the outer electrode surface but at the FTO CoBP interface.

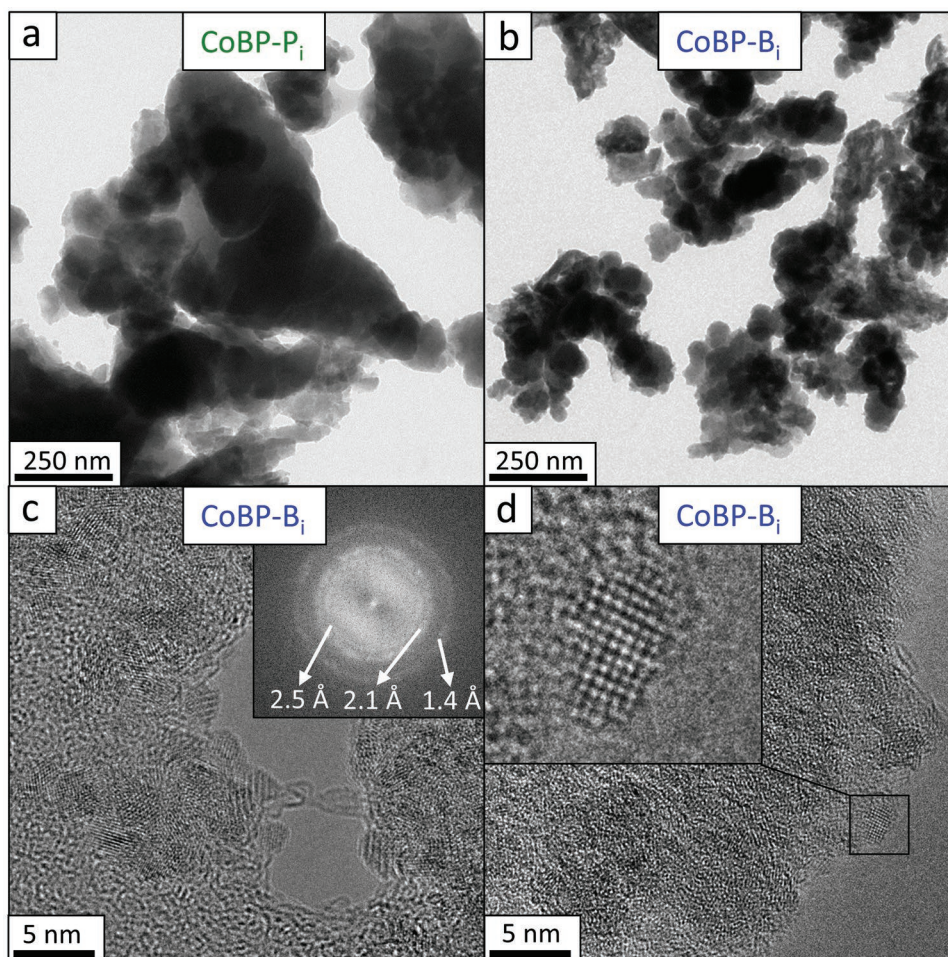


Figure 4. a–d) TEM images of $\text{Co}(\text{H}_2\text{O})_2[\text{B}_2\text{P}_2\text{O}_8(\text{OH})_2]\cdot\text{H}_2\text{O}$ (CoBP) scratched off from FTO after 24 h OER CP (1 mA cm^{-2}) in 0.1 M KP_i or KB_i buffer. (a) and (b) reveal that the particles of CoBP-P_i are significantly larger than those of CoBP-B_i . In contrast to CoBP-P_i , for CoBP-B_i , atomic columns of stacking crystalline domains could be resolved in (c) and (d). The inset in (c) shows the fast Fourier transform of (c) revealing three lattice distances (1.4, 2.1, and 2.5 Å). These distances are assigned to lattice planes of a CoCat structural model in Figure 8b,c. More TEM images and SAEDs of the same compounds can be found in Figures S21–S25, Supporting Information.

constituting elements for both CoBP-P_i and $-\text{B}_i$ after 24 h CP (Figures S17–S20, Supporting Information).

TEM images of CoBP-P_i and $-\text{B}_i$ show that the morphology after 24 h CP is a function of the buffer and that CoBP-B_i comprises smaller particles (10–250 nm) than CoBP-P_i (50 nm to several μm , Figure 4a,b and Figures S21 and S22, Supporting Information). Another difference between the phases can be seen in the SAED (Figure S23, Supporting Information): for CoBP-P_i , no clear diffraction rings are present, but for CoBP-B_i rings can be seen. Thus, CoBP-B_i has a higher degree of long-range order and might be best described as nanocrystalline. This trend is confirmed by high-resolution (HR)-TEM. For CoBP-P_i , spherical aberration corrected HRTEM with a field emission gun cathode and a point resolution of 75 pm could not resolve any lattice fringes or atom columns (Figure S21, Supporting Information, for a beam damage discussion see Figure S24, Supporting Information). However, for CoBP-B_i , the same machine was capable to resolve atomic columns of probably orderly stacking crystalline domains of 1.5–3 nm

(Figure 4c,d and Figure S25, Supporting Information). The fast Fourier transformed (FFT) of these images uncover three different lattice spacings of the one which is equivalent to the diffraction ring of the SAED (Figure 4c and Figure S23, Supporting Information). All three distances from the FFT could be assigned to lattice planes in the domains of edge sharing $[\text{CoO}_6]$ octahedra (see Section 2.4.3).

2.3. Comparison of the Reconstruction of CoBP with CoO and Co_3O_4 under (Near-)Neutral OER Conditions

As we found that CoBP reconstructs completely under the herein applied OER conditions, we decided to investigate whether the cobalt oxide phases, CoO (rock salt structure) and Co_3O_4 (spinel structure), behave similarly. In the first hours of the CP measurements, for CoBP, the potential to reach 1 mA cm^{-2} decreases indicating the continuous formation of an OER active phase. In contrast, for both

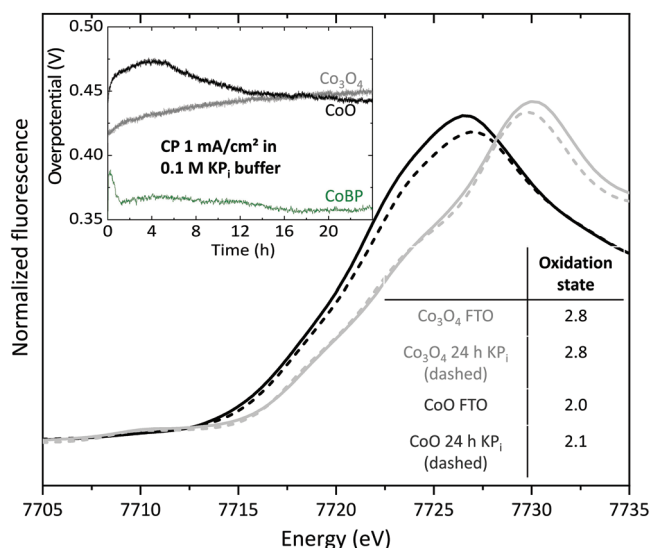


Figure 5. OER quasi in situ and ex situ Co K-edge XANES data of CoO (rock salt structure) and Co₃O₄ (spinel structure). The inset shows the *iR*-corrected CP (1 mA cm⁻²) data of both oxides with CoBP as reference in 0.1 M KP₁ (pH 7.20). The quasi in situ samples (dashed lines) were freeze-quenched at $\eta = 400$ mV after 24 h CP at 1 mA cm⁻². Figure S10, Supporting Information, shows the linear regression used to determine the oxidation states.

oxides, an increase in the required potential is observed at the beginning (Figure 5 inset). Furthermore, after 24 h, the η_1 is almost 100 mV lower for CoBP-P_i compared to the two oxides with the same cobalt loading. These differences imply that the behavior of the oxides is substantially different. In this regard, quasi in situ XANES reveals a slight increase in the average oxidation state for CoO and an unchanged oxidation state for Co₃O₄ (Figure 5). Further, the smaller edge maximum for both oxides after the OER treatment indicates a minor amorphization. The quasi in situ EXAFS spectra of CoO and Co₃O₄ after 24 h of OER could be fitted well with the crystal structures of the pristine materials (Figure S26 and Tables S3 and S4, Supporting Information). Thus, cobalt oxides are more reluctant toward amorphization during OER than CoBP.

2.4. Electrochemical, Structural, and Morphological Analysis of CoBP-P_i, CoBP-B_i, CoP_i, and CoB_i

2.4.1. OER Activity

To investigate the influence of the catalyst type on the OER, the four amorphous CoCat phases (Figure 6a for an overview) together with the two crystalline cobalt oxides were tested in 0.1 M KP₁ buffer for 24 h at a low current density, 1 mA cm⁻² (Figure S27, Supporting Information, all electrodes had a cobalt loading of 1.6 ± 0.2 μ mol determined by ICP-OES). Their activity declines in the order CoBPB_i > CoBP_i \approx CoB_i > CoP_i > CoO \geq Co₃O₄. To check the influence of the buffer and its concentration during catalysis, Tafel slopes were recorded in 0.1 M and 1 M KP₁ and KB_i using the most

active catalyst, CoBP-B_i (Figure S28, Supporting Information). At 0.1 M, no significant difference between KP₁ and KB_i were observed; nevertheless, 1 M KB_i buffer yields higher current densities and a wider Tafel range than 1 M KP₁ (for more information on the different buffers, *iR* correction, and stirring see Figures S28 and S29, Supporting Information). Thus, we decided to continue our studies in stirred 1 M KB_i. Steady-state current–voltage graphs of CoBP-P_i, CoBP-B_i, CoP_i, and CoB_i were obtained by *iR*-corrected 3 min CA measurements at various potentials (Figure 6b). This data was also used to determine the Tafel slopes (Figure 6c) of all four compounds and normalized by the number of electrons transferred in the reduction peak (Figure 6d, see Section 2.5.1 and the therein discussed Figures S36–S38, Supporting Information, for more information). Under these conditions, again, CoBP-B_i is most OER active and the Tafel slopes of the catalysts formed in KB_i buffer show similar Tafel slopes (around 56 mV dec⁻¹), which are lower than those of the catalysts formed in KP₁ buffer (around 68 mV dec⁻¹). It is noticeable that previous reports described the Tafel slope of CoP_i and CoB_i to be around 59 mV dec⁻¹ (correlating to $2.3 \times RT/F$);^[12,33] however, when taking a closer look at the Tafel data of ref. [12] differences between the slopes of CoP_i and CoB_i are clearly visible. Furthermore, other groups have reported different slopes than 59 mV dec⁻¹ for various CoCat phases already.^[34,35]

Three trends concerning the activity can be deduced:

1. Considering the precursors, the activity follows the trend CoBP > Co²⁺_{aq} > CoO/Co₃O₄.
2. Considering the buffer during (trans)formation, the catalysts formed in KB_i are more active and have lower Tafel slopes than those formed in KP₁, for example, CoBPB_i > CoBPP_i and CoB_i > CoP_i.
3. Considering the buffer used as electrolyte during catalysis, higher buffer concentrations are beneficial and KB_i buffer yields the highest current densities at a concentration of 1 M.

2.4.2. ICP-OES

To understand how much phosphate and borate is in the respective four catalysts and if these species exchange during catalysis, all four catalysts were subjected to CP (1 mA cm⁻², 24 h) measurements in 0.1 M KP₁, 0.1 M KB_i, and 1 M KB_i electrolyte and their Co, B, P, and K ratio were investigated by ICP-OES (Table 1). The following trends can be deduced:

1. Before being subjected to a new buffer, catalysts formed in 0.1 M KP₁ (CoBP-P_i and CoP_i) contain only P_i, and catalysts formed in 0.1 M KB_i (CoBP-B_i and CoB_i) contain only borate species.
2. Catalysts formed in KP₁ contain more than the doubled molar amount of buffer species and potassium than those reconstructed in KB_i.
3. After complete reconstruction to CoP_i, the phosphate groups cannot be exchanged by operating in KB_i buffer; however, borate is exchanged by phosphate when operating in KP₁ buffer.

This data indicates that the chemical nature of the formed catalyst mainly depends on the buffer it was reconstructed in and not on the precursor (CoBP or Co²⁺_{aq}).

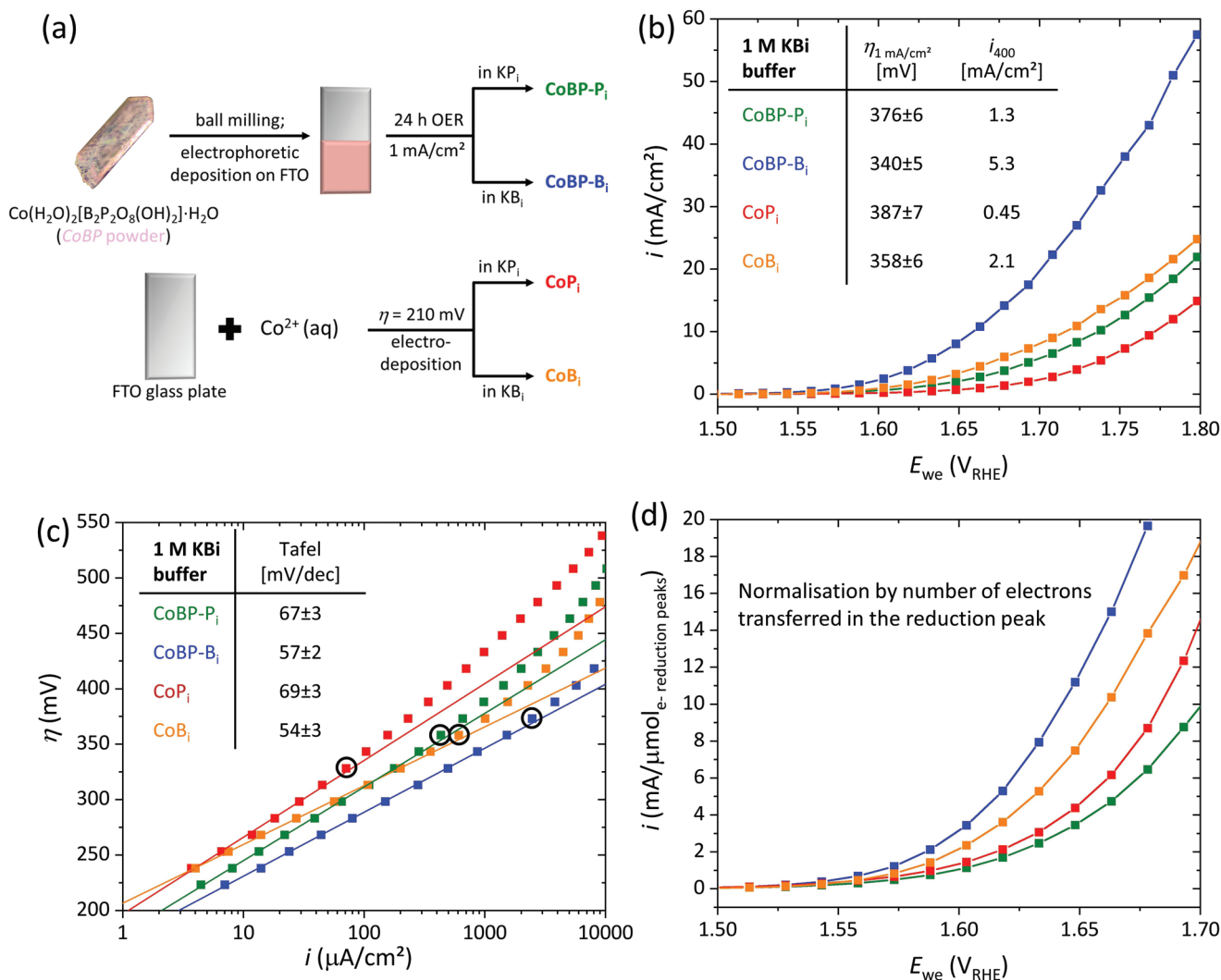


Figure 6. a) Overview showing how the four herein compared catalysts were obtained. b) Steady-state potential–current graph obtained from CA measurements (3 min per point, stirring 600 rpm, iR -corrected, see Figures S28 and S29, Supporting Information, for more information on the iR correction and stirring, i_{400} represents the current density at an overpotential of 400 mV) of the four catalysts (cobalt loading of $1.6 \pm 0.2 \mu\text{mol}$) shown in (a) in 1 M KB_i . c) Tafel plots of the same data as shown in (b), the black circles mark the first point that deviates from the linear Tafel range. d) The data of (b) normalized by the number of electrons transferred in the reduction peak (more information can be found in Section 2.5.1 and the therein discussed Figures S36–S38, Supporting Information). The straight lines in graphs (b) and (d) should guide the reader's eye and have no physical meaning.

2.4.3. Quasi In Situ XAS

To gain further insights into the catalyst structure during OER, we performed quasi in situ XAS measurements on all catalysts (CA at $\eta = 400 \text{ mV}$, Figures 7 and 8a). For all systems, XANES reveals a quasi in situ bulk cobalt oxidation state of 3.2 (Figure 7) and an ex situ oxidation state of 2.9 (Figure 7). These oxidation states are in line with the ones reported ex- and quasi in-situ for CoCat materials.^[30]

For all catalysts, the quasi in situ cobalt K-edge Fourier transformed EXAFS spectra indicate a layered structure formed by edge sharing $[\text{CoO}_6]$ octahedra (Figure 8a–c and Figure S30, Supporting Information), as reported for CoP_i and CoB_i (CoCat materials in general) previously.^[6–8] To gain deeper insights and to identify structural differences between the compounds, all spectra were simulated. The model used

is based on five coordination shells (Figure 8b). All spectra could be simulated well based on this model (a simulation considering multiple scattering effects and one without is provided in Tables S5 and S6, Supporting Information). The radii of the five shells showed only minor variations between the different compounds confirming the structural model of Figure 8b, which is also consistent with the observed lattice distances of the TEM data (Figure 4). In contrast to the radii, the populations of the Co–Co shells differ between the catalysts formed in KB_i (larger populations) and KP_i (Figure 8d,e). The size of a domain, a layer of edge sharing $[\text{CoO}_6]$ octahedra (Figures 1 and 8b), correlates with the population of the Co–Co shells (for domains of different sizes and their respective populations see Figure S31 and Table S1, Supporting Information). Thus, catalysts formed in KB_i have larger domain sizes ($\approx 2\text{--}3.2 \text{ nm}$) than those formed in KP_i ($\approx 0.6\text{--}1.4 \text{ nm}$), as

Table 1. Molar ratios of Co, B, P, and K of various catalysts tested in different buffers. The ICP results were always taken after 24 h at 1 mA cm⁻² in the respective buffer. For example: for CoBP-P_i in 0.1 M KP_i, CoBP deposited on FTO was reconstructed by CP (1 mA cm⁻², 24 h) in 0.1 M KP_i yielding CoBP-P_i, washed with demineralized water (rinsing 10 s), and then the complete film dissolved in aqua regia and measured by ICP-OES. For CoBP-P_i in 0.1 M KB_i, CoBP deposited on FTO was reconstructed by CP (1 mA cm⁻², 24 h) in 0.1 M KP_i yielding CoBP-P_i, then the sample was washed with demineralized water and subsequently a CP (1 mA cm⁻², 24 h) in 0.1 M KB_i was performed, followed by washing, dissolution, and the ICP-OES measurement.

Catalyst	Buffer	Co	B	P	K
CoBP-P _i	0.1 M KP _i	1.00	0.00	0.45	0.45
	0.1 M KB _i	1.00	0.03	0.43	0.46
	1 M KB _i	1.00	0.06	0.43	0.51
CoBP-B _i	0.1 M KP _i	1.00	0.03	0.15	0.24
	0.1 M KB _i	1.00	0.17	0.00	0.19
	1 M KB _i	1.00	0.16	0.00	0.19
CoP _i	0.1 M KP _i	1.00	0.00	0.36	0.41
	0.1 M KB _i	1.00	0.04	0.33	0.38
	1 M KB _i	1.00	0.17	0.35	0.38
CoB _i	0.1 M KP _i	1.00	0.01	0.10	0.23
	0.1 M KB _i	1.00	0.08	0.00	0.18
	1 M KB _i	1.00	0.11	0.00	0.17

also previously identified in several comparisons of CoP_i and CoB_i.^[6–8]

A detailed discussion of the domain size and the EXAFS models can be found in the caption of Table S1, Supporting

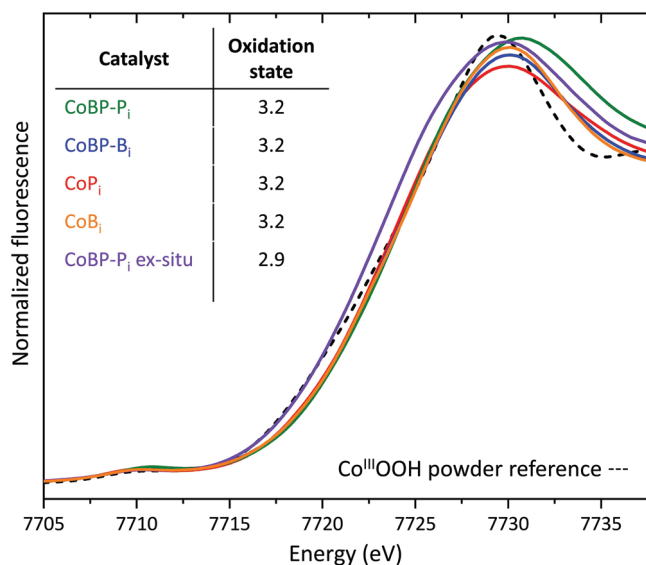


Figure 7. OER quasi in situ Co K-edge XANES data of the four catalysts shown in Figure 6a and one ex situ measurement as comparison together with a cobalt(III) reference (CoOOH). The quasi in situ samples (dashed lines) were freeze-quenched at $\eta = 400$ mV after 24 h CP at 1 mA cm⁻² in KB_i buffer. Figure S10, Supporting Information, shows the linear regression used to determine the oxidation states. Data of the same catalysts freeze-quenched in KP_i buffer shows no significant differences (Figure S32, Supporting Information).

Information. A domain can be viewed as a nanosized crystallite and larger crystallites enable diffraction. Thus, the observation of electron diffraction for CoBP-B_i and its absence for CoBP-P_i (Figure 4 and Figure S21, Supporting Information) is consistent with the EXAFS data. Further, in contrast to CoBP-P_i, for CoBP-B_i, HR-TEM could directly visualize atomic columns of domains that probably stack in an ordered way (Figure 4).

After the initial formation, OER tests in different buffers for 24 h were performed. These tests did not change the XANES and EXAFS spectra of these catalysts (Figures S32–S34, Supporting Information) showing that the structures remain after initial formation under the investigated conditions.

2.4.4. SEM

To identify differences in the morphology and surface area of the four catalysts, SEM images were taken of the catalyst films with the same cobalt loading (Figure 9). These images reveal large differences in the morphology of the films. CoP_i has a comparably flat surface, and its film shows no porosity on the nanometer scale. CoBP-P_i's surface is not flat and it consists of spherical particles with a diameter of several hundred nanometers. CoB_i also consists of spherical particles, but with a smaller size than those of CoBP-P_i. CoBP-B_i still contains spherical particles but is of a much smaller size than CoB_i. CoBP-B_i has by far the highest surface area. Furthermore, its film with the same loading is at least two times thicker than the other ones emphasizing its larger porosity. In this regard, it is noticeable that the as-deposited CoBP film (Figure S7, Supporting Information) is thicker than the CoBP-P_i and CoBP-B_i films formed from it. Additionally, the TEM investigation of CoBP-P_i and CoBP-B_i (Figure 4 and Figures S21 and S22, Supporting Information) shows a significantly smaller particle size for CoBP-B_i consistent with the SEM investigations.

2.4.5. Differences between CoBP-P_i, CoBP-B_i, CoP_i, and CoB_i

The OER activity follows the trend CoBP-B_i > CoBP-P_i ≈ CoB_i > CoP_i. The atomic structure of the systems is determined by the buffer used during the formation, whereas catalysts formed in KP_i have smaller domain sizes and contain more buffer species while those formed in KB_i have larger domain sizes and less buffer species. The morphology of the catalysts is affected by the precursor type and the buffer used during the formation, whereas Co²⁺ precursor and KP_i buffer leads to smaller particles while CoBP precursor and KB_i buffer leads to larger ones and flatter films.

2.5. Factors for the Different OER Activities of CoBP-P_i, CoBP-B_i, CoP_i, and CoB_i

In this section, we first describe the different parameters used to measure the OER performance and interconnect them with the observables and models explaining the performance variations. In the end, we discuss which aspects are most relevant for the direct comparison of the four catalysts.

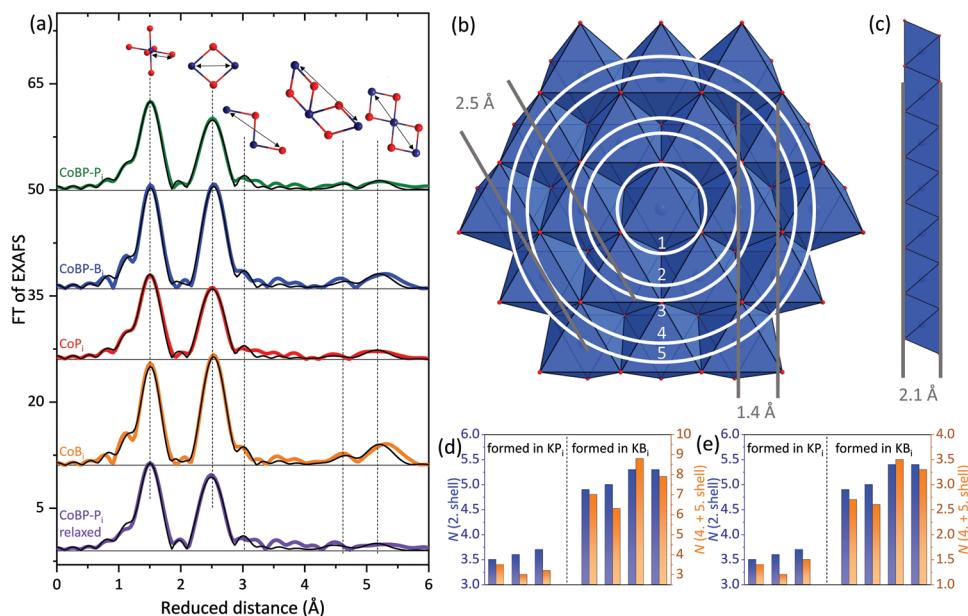


Figure 8. a) OER quasi in situ Co K-edge Fourier transformed EXAFS plots of the four catalysts shown in Figure 6a and one ex situ measurement as comparison. The quasi in situ samples were freeze-quenched at $\eta = 400$ mV after 24 h CP at 1 mA cm^{-2} in KB_i buffer. Data of the same catalysts freeze-quenched in KP_i buffer shows no significant differences (Figures S33 and S34, Supporting Information). The most important distances with their structural motifs are depicted by the dashed vertical lines. The black curves show the simulation. EXAFS simulation parameters and experimental data in k -space are provided in Figure S30 and Table S5, Supporting Information. b) A domain of a CoCat-like structure. The white rings represent the five distances marked with dashed lines in (a). The gray lines mark the lattice planes that fit to the distances observed in the HRTEM (Figure 4). c) Side view of a domain with the missing distance from the HRTEM (Figure 4) with gray lines representing oxygen lattice planes. d,e) The population numbers of the second coordination shell and the sum of the fourth and fifth coordination shell all shown in (b). The larger these populations are, the bigger is the average domain size (Figure S31 and Table S1, Supporting Information) and the higher the degree of order.^[24,30] For (d) no multiple scattering was considered while for (e) a multiple scattering analysis was performed for the second coordination shell. Table S1, Supporting Information, includes a more detailed discussion of the two approaches with respect to the domain size. Table S6, Supporting Information, shows the simulation parameters including multiple scattering.

2.5.1. Formation in KP_i versus KB_i : Interconnecting Tafel Slope, Redox Peaks/Activity, Long-Range Order, and Buffer Binding

Even though, all catalysts possess the same short-range order, the two catalysts formed in KB_i buffer (CoB_i and CoBP-B_i) have a lower Tafel slope than those formed in KP_i (CoP_i and CoBP-P_i). This variation reveals differences in the active sites and

reaction mechanisms of the catalysts. Recently, Bergmann et al. have identified a unified structural motif of $\text{Co}_x\text{O}_y\text{H}_z$ OER catalysts that is consistent with the domain edge sites of the herein described catalysts' structures (Figure 1).^[36] Furthermore, Bergmann et al. showed that the number of edge sites correlates to the ratio of the current density at the $\text{Co}^{\text{II/III}}$ and $\text{Co}^{\text{III/IV}}$ reduction peak minima (only accessible edge sites contribute to the

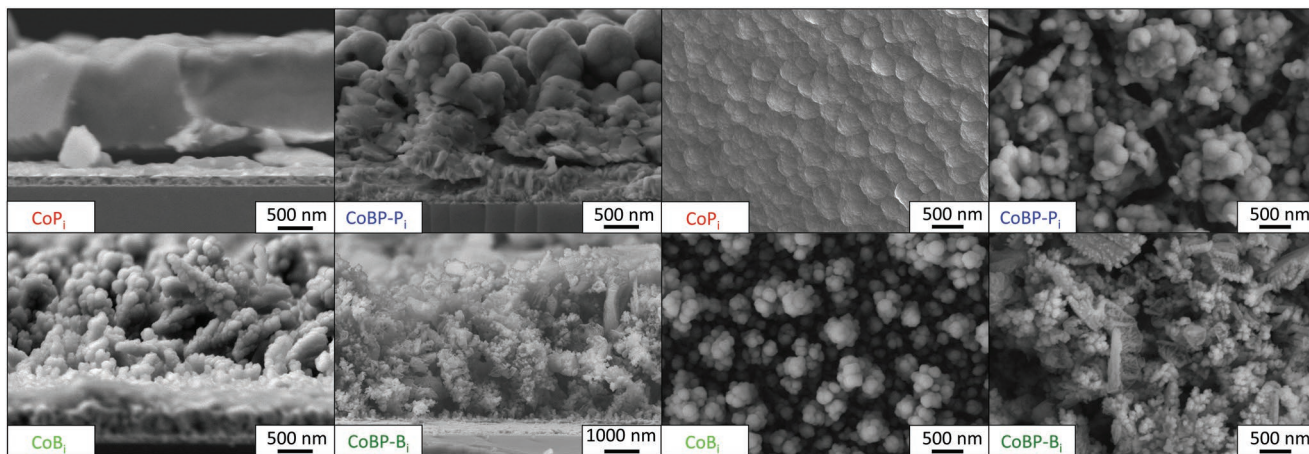


Figure 9. SEM cross-sectional images of all four catalysts shown in Figure 6a (left four images) and images with an orthogonal viewing direction on the film of the same catalysts. Stark differences in the morphology and surface area are present.

Co^{II/III} redox activity) and that a higher ratio of edge sites results in lower Tafel slopes.^[36] Therefore, we recorded CVs of all four compounds (Figures S35–S37, Supporting Information). While the samples reconstructed in KP_i showed the same current density at the Co^{II/III} and Co^{III/IV} reduction peak minima, the samples formed in KB_i buffer showed a larger current density at the Co^{II/III} reduction-peak minima than the Co^{III/IV} one. This observation is consistent with the smaller Tafel slope that was obtained for samples formed in CoB_i.

As elaborated, the electrochemical data suggests that CoB_i and CoBP-B_i have more Co^{II/III} redox active edge sites than CoP_i and CoBP-P_i. Our EXAFS analysis and previously reported pair distribution function analyses imply a smaller domain size for catalysts formed in KP_i buffer compared to those formed in KB_i,^[6–8] probably because P_i binds strongly at the edge sites inhibiting the further domain growth.^[37] A smaller domain size correlates to more edge sites and thus should result in a higher Co^{II/III} redox activity, better OER performance, and a lower Tafel slope.^[38] To understand this apparent contradiction, the different binding modes of phosphate and borate on the catalysts' edge sites must be considered (for a detailed discussion and reaction mechanism see Figure S37, Supporting Information).^[35,37,39] As our ICP-OES results of Table 1 and previous reports have shown, P_i binds strongly and under our OER conditions irreversibly to the [CoO₆] domain edge sites, while B_i can easily be dissociated (Figure S39, Supporting Information).^[37] The oxygen atoms of the phosphate group replace hydroxides in μ₂-OH-bridged Co^{III} moieties. Thus, P_i binding hinders redox activity of these sites by disabling deprotonation in the proton-coupled electron transfer^[40] and consequently inhibits their OER activity. We note that the catalysts reconstructed in KP_i also contain twice as many buffer species than those reconstructed in KB_i (Table 1) and that the phosphate groups of KP_i remain in the catalyst during catalysis, in contrast to the borate ions of KB_i that exchange, when operated in KP_i buffer (Table 1). Thus, for the herein discussed cases, the inhibition by the buffer binding dominates the effect of the domains size on OER available edge sites.

2.5.2. Total Number of Redox Active Sites

Herein, in regimes where mass-transport limitations are negligible, catalysts with the same Tafel slope (same ratio of Co^{II/III} to Co^{III/IV} redox active sites, e.g., CoP_i and CoBP-P_i) show different OER activities at the same loading (Figure 6b,c). These variations must originate from differences in the number of OER active sites per total cobalt loaded on the substrate. As OER active sites must be able to change their redox state during catalysis, the number of electrons transferred in the reversible Co^{II/III} and Co^{III/IV} redox peaks (e^-_{redox}) has often been found to be proportional to the number of OER active sites (in the previous paragraphs, the ratio of the Co^{II/III} and Co^{III/IV} redox active sites was considered not their total number). e^-_{redox} qualitatively follows the trend of the four catalysts' activities (for two kinds of normalizations see Figures S36–S38, Supporting Information). Thus, it is one aspect to explain the activity differences between the samples formed in the same electrolyte (same Tafel slope). However, a normalization of the activity data

by this quantity shows still significant differences revealing that other effects are also important, as described in the previous and following paragraphs.

2.5.3. Morphology: Surface Site versus Bulk Site Activity

A previous report on the difference between the bulk activity of CoP_i compared to its surface activity (around 15 nm) showed that the surface activity is higher per loaded cobalt atom; nevertheless, at high catalysts loadings, the bulk activity dominates, as dramatically more cobalt sites are in the bulk compared to the surface.^[10] We suggest that the difference in the activity between bulk and surface cobalt site does not mainly originate from different natures of active sites, as 1) no structural differences between the near-surface and the bulk phase has been observed,^[10,11] as 2) the Tafel slopes and CV shapes of thin near-surface activity dominated CoP_i films are the same as those of films more than a magnitude thicker,^[12,41] and as 3) we could only observe a small difference between the Tafel slope of a CoP_i film with a loading of 0.04 μmol compared to 1.6 μmol (Figure S40, Supporting Information). The SEM images (Figure 9) show remarkable differences in the morphologies and surface areas (catalyst–electrolyte interface) of the four catalysts. The catalysts with a larger surface area will benefit from the higher activity of the surface cobalt sites. In agreement with this, the surface area trend found herein agrees with the OER activity trend, even in regimes where mass transport is negligible. We note here that meaningful double layer (C_{dl}) or electrocatalytic active surface area (ECSA) measurements are challenging to obtain of these catalysts and are not reported herein or in the literature (for a detailed discussion see Figure S41, Supporting Information). Furthermore, compared to (near-)surface active catalysts, surface area normalizations are not suitable to obtain an intrinsic activity and the surface area is poorly defined and not straightforwardly connected to the catalytic performance in general, as within the whole electrolyte-permeable catalyst an interface between electrolyte/substrate and active sites exists and not only on the outer surface.

2.5.4. Mass Transport: Linear Tafel Range and Surface Area

The discussion of intrinsic activity and the number of active sites in the last two subchapters focused on low current densities, where mass transport is negligible, as linear Tafel slopes are still preserved. However, at higher current densities, such limitations can inhibit the OER.^[11,12,41–44] Mass-transport limitations can arise from insufficient electron transport or proton transport (as well as oxygen bubble detachment which is not discussed herein). Recently, it has been proven by quasi in situ conductivity measurements that electron transport is not a limiting factor.^[12] However, proton transport has been found to be a limiting factor in various previous reports.^[11,12,41,42] In a stirred setup (Figure S29, Supporting Information), it can arise

1. In the electrolyte or electrode–electrolyte interface in form of a low-pH zone (pH gradient);^[42,43,45,46]
2. Within the catalyst film.^[12,41]

Concerning (1), at higher potentials, we could observe an activity increase when using 1 M instead of 0.1 M KB_i (Figure S29, Supporting Information) indicating buffer dependent proton-transport limitations. ICP-OES (Table 1) shows that the buffer concentration inside the film does not significantly increase when the electrolyte concentration is changed from 0.1 to 1 M KB_i . Thus, (2) should not depend on the buffer concentration, and (1) must be responsible for the buffer concentration dependency of the activity. Regarding (1), in the simplest diffusion model of a stirred electrocatalytic solution, the stirred bulk solution has a constant concentration of all constituents and on the surface of the electrode exists a diffusion layer.^[45,46] A higher buffer concentration will increase the concentration of proton carriers in this diffusion layer explaining the observed dependency. Alternatively, a valid explanation is also that the proton exchange between the catalyst film and the electrolyte buffers is the rate limiting step of the proton transport and that it depends on the buffer concentration.

Concerning (2), as such limitations will be the only ones that depend on the catalyst film thickness, they can be proven by comparing the linear Tafel range of two electrodes with different loadings (Figure S40, Supporting Information). The linear Tafel range for CoP_i catalysts with a lower loading extends to current densities that are over a magnitude larger than those of CoP_i catalysts with 40-times higher loading. This comparison suggests that proton transport within the catalysts is also an important factor.

The proton mass transport of (1) and (2) can both be improved by increasing the surface area/outer catalyst–electrolyte interface. This conclusion explains why CoBP-B_i is considerably more active at higher current densities and has a wider Tafel range than the other catalysts (Figure 6c), as CoBP-B_i has the highest surface area (Figure 9). In general, the Tafel range (Figure 6c) and the surface area (Figure 9) of the catalysts show the same trend.

2.5.5. Explanation of the Activity Difference of CoBP-P_i , CoBP-B_i , CoP_i , and CoB_i

Figure 10 summarizes the parameters causing the activity differences found between the four herein investigated catalysts. Catalysts formed from CoBP precursor are more active than those formed from Co^{2+} due to their different morphology that creates a larger surface area (interface between the bulk electrolyte and outer catalyst) for CoBP derived systems. This difference leads to more surface sites, which have been shown to be more active than bulk sites,^[10] and is beneficial for proton transport. Catalysts formed in KB_i buffer are more active than those formed in KP_i buffer, 1) due to differences in the morphology resulting in a larger surface area for KB_i derived phases and 2) due to more accessible edge sites, as P_i irreversible binds to edge sites leading to their inhibitions. Concerning point (2), it is worth mentioning that KB_i -derived phases have a larger domain size than KP_i derived ones, which results in less edge sites; however, the effect on available edge sites is dominated by the P_i binding. Note that KP_i derived phases have a molar Co to P_i ratio of around 1–0.4. Thus, even if every second cobalt site is on the edge, 80% of these sites could be inhibited by KP_i .

2.6. An Optimized System Operating Efficiently and Long-Term Stable at High Current Densities at Elevated Temperature

Due to the mass-transport limitations and inferior kinetics of the OER in near-neutral media compared to a strongly alkaline and acidic one, it is challenging to achieve high current densities at reasonable overpotentials.^[14,47] Taking our best catalysts (CoBP-B_i) and considering our deduced concepts and previous reports,^[44,48–50] we performed the following optimizations of our system to meet this challenge:

1. Loading the catalyst on porous nickel foam.
2. Increasing the cobalt loading to $22 \mu\text{mol cm}^{-2}$.
3. Raising the buffer concentration to 4 mol kg^{-1} .
4. Elevating the temperature to $65 \text{ }^\circ\text{C}$.

Comparing this system to CoP_i and CoBP-B_i at room temperature on FTO (**Figure 11a**), we achieved an activity increment of around 475-times (CoP_i) and 40-times (CoBP-P_i) at $1.625 \text{ V}_{\text{RHE}}$. The optimized system reaches 100 mA cm^{-2} at $1.585 \text{ V}_{\text{RHE}}$ which is still inferior but in range of the most active OER catalysts in strongly alkaline and acidic media under steady-state conditions.^[4,47,51,52] In general, these results show that the gap between near-neutral and strongly alkaline and acidic OER is likely to decrease at elevated temperatures, as those temperatures partly compensate the proton-transport disadvantage of buffers compared to hydroxide and protons.^[44,53] Furthermore, the solution resistance is decreased (Figure S28c, Supporting Information) and the autoprotolysis of water is enhanced.^[54]

Long-term stability at higher potentials is a critical issue, as, in near-neutral media, cobalt-based catalysts rely on a self-healing mechanism, which prevents complete dissolution of the catalyst by continuous redeposition (but see also ref. [55]).^[56] We tested the long-term stability of our optimized system at a current density of 250 mA cm^{-2} at $65 \text{ }^\circ\text{C}$ for 1 month (Figure 11b). During the CP measurement, this current density was achieved at $1.62 \pm 0.03 \text{ V}_{\text{RHE}}$ without any observable degradation of the activity over 1 month proving that long-term stable, near-neutral water splitting at elevated temperatures, high efficiencies, and industrially relevant current densities is realizable.

3. Conclusion

Herein, we have synthesized the cobalt borophosphate, CoBP , and, for the first time, investigated toward its OER activity. Our ex- and quasi in-situ analysis uncover an unreported kind of reconstruction of this material which does not start at the outer surface of the electrode but at the FTO– CoBP interface. After a prolonged time, CoBP could be fully reconstructed into two different CoCat phases depending on the buffer (CoP_i or CoB_i) that are significantly more OER active than CoP_i and CoB_i under the same conditions (Figure 6a for an overview). With these four different CoCat phases, we performed a detailed electrochemical, structural, and morphological analysis enabling us to answer the research question (1)–(4) of the introduction:

1. Both the precatalyst type and the nature of the buffer used during the reconstruction are relevant for the OER activity

Reconstruction from CoBP compared to $\text{Co}^{2+}_{(\text{aq})}$
strongly enhances the surface area

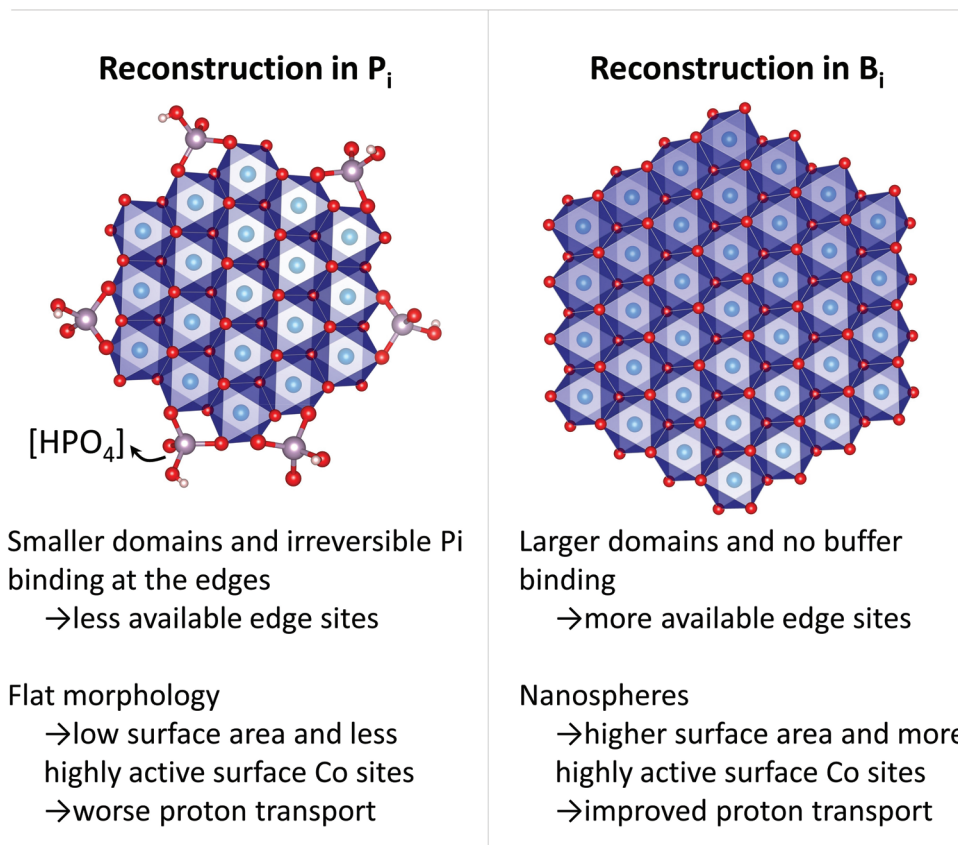


Figure 10. Summary of the factors causing the activity difference of the four herein investigated fully reconstructed catalysts, which were obtained either in KPi or KB_i electrolyte and either from $\text{Co}^{2+}_{(\text{aq})}$ or CoBP as precatalyst. The blue spheres are the cobalt atoms, the red ones oxygen, the purple–gray ones phosphorus, and the light-pink ones hydrogen.

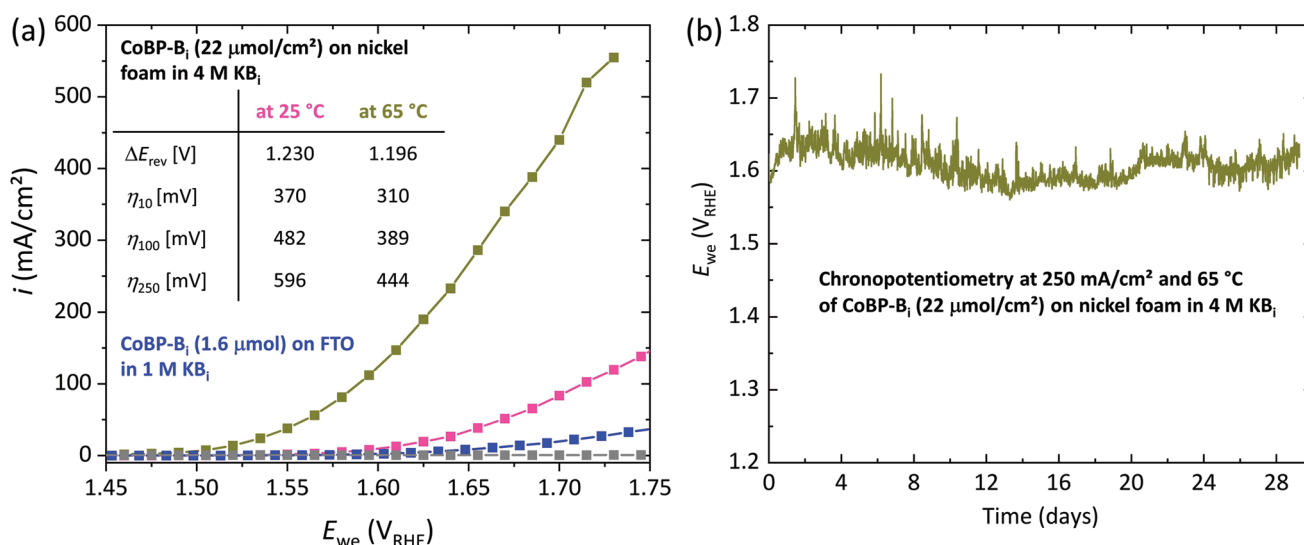


Figure 11. OER performance of CoBP- B_i on nickel foam operating at elevated temperature and high current densities in 4 mol kg^{-1} KB_i electrolyte (pH = 9.24 at 25 °C). a) Steady-state potential–current graph obtained from CA measurements (3 min per point, stirring 600 rpm, iR -corrected, see Figures S28 and S29, Supporting Information, for more information on the iR correction and stirring) of CoPi and CoBP- B_i on FTO (1.6 $\mu\text{mol}/\text{cm}^2$) and CoBP- B_i on nickel foam (22 $\mu\text{mol}/\text{cm}^2$). The gray data points are from bare nickel foam at 25 °C in the same electrolyte. b) Long-term stability measurement of CoBP- B_i on nickel foam.

of the finally formed CoCat phase. The precatalysts only influence the morphology and surface area, whereas the nature of the buffer determines the long-range order, and, depending on its nature, it binds irreversibly to the catalyst edge sites.

- We identified the following reasons for the different activities: (a) different numbers of accessible edge sites with high OER activities compared to the total cobalt loading (identified by $\text{Co}^{\text{II/III}}$ redox activity and affecting the Tafel slope); (b) inhibition of active edge sites by irreversible buffer binding, (c) different morphologies and surface areas whereas, in general, surface cobalt sites are more active than bulk cobalt sites, and, at higher current densities, they are less affected by proton mass-transport limitations.
- Proton mass transport (a) in the electrolyte/at the catalyst–electrolyte interface and (b) within the catalyst films is limiting the activity at higher loadings and current densities. Both can be minimized by increasing the surface area and operating temperature while (a) can also be reduced by increasing the buffer concentration.
- Using the herein derived concepts, we constructed an optimized OER electrode that could maintain a current density of 250 mA cm^{-2} at $65 \text{ }^\circ\text{C}$ at a potential of $1.62 \pm 0.03 \text{ V}_{\text{RHE}}$ while operating in (near-)neutral pH and at $65 \text{ }^\circ\text{C}$. This performance is still inferior for practical application but in the range of the most active OER catalysts in strongly alkaline and acidic media.

While achieving a high activity and remarkable stability for the OER, this work conclusively explains the activity differences between the four investigated CoCat phases and due to the structural similarity, we anticipate that those concepts should also be applicable not only to cobalt oxyhydroxides but also to nickel and iron oxyhydroxides.

Supporting Information

Supporting Information is available from the Wiley Online Library or from the author.

Acknowledgements

The authors are grateful to the Einstein Center of Catalysis (EC2) for financial support. This project was also funded by the Deutsche Forschungsgemeinschaft (DFG, German Research Foundation) under Germany's Excellence Strategy – EXC 2008/1 – 390540038–UniSysCat and the German Federal Ministry of Education and Research (BMBF project “PrometH2eus,” 03HY105C). P.W.M. greatly acknowledges support from the German Federal Ministry of Education and Research in the framework of the project Catlab (03EW0015A/B). H.D. acknowledges financial support from BMBF (Operando XAS, 05K19KE1). The authors would like to thank Dr. I. Zaharieva for the initial XAS data collection.

Open access funding enabled and organized by Projekt DEAL.

Conflict of Interest

The authors declare no conflict of interest.

Data Availability Statement

The data that support the findings of this study are available from the corresponding author upon reasonable request.

Keywords

cobalt borophosphate precatalysts, cobalt oxyhydroxides, edge sites, (near-)neutral oxygen evolution reaction, precatalyst reconstructions, proton transport, water oxidation

Received: August 17, 2022

Revised: September 15, 2022

Published online: November 4, 2022

- X. Zheng, B. Zhang, P. De Luna, Y. Liang, R. Comin, O. Voznyy, L. Han, F. P. García de Arquer, M. Liu, C. T. Dinh, T. Regier, J. J. Dynes, S. He, H. L. Xin, H. Peng, D. Prendergast, X. Du, E. H. Sargent, *Nat. Chem.* **2018**, *10*, 149.
- D. G. Nocera, *Acc. Chem. Res.* **2012**, *45*, 767.
- J. Herranz, A. Pătru, E. Fabbri, T. J. Schmidt, *Curr. Opin. Electrochem.* **2020**, *23*, 89.
- N. Wang, Z. Cao, X. Zheng, B. Zhang, S. M. Kozlov, P. Chen, C. Zou, X. Kong, Y. Wen, M. Liu, Y. Zhou, C. T. Dinh, L. Zheng, H. Peng, Y. Zhao, L. Cavallo, X. Zhang, E. H. Sargent, *Adv. Mater.* **2020**, *32*, 1906806.
- J. N. Hausmann, R. Schlögl, P. W. Menezes, M. Driess, *Energy Environ. Sci.* **2021**, *14*, 3679.
- G. Kwon, H. Jang, J.-S. Lee, A. Mane, D. J. Mandia, S. R. Soltau, L. M. Utschig, A. B. F. Martinson, D. M. Tiede, H. Kim, J. Kim, *J. Am. Chem. Soc.* **2018**, *140*, 10710.
- P. Du, O. Kokhan, K. W. Chapman, P. J. Chupas, D. M. Tiede, *J. Am. Chem. Soc.* **2012**, *134*, 11096.
- C. L. Farrow, D. K. Bediako, Y. Surendranath, D. G. Nocera, S. J. L. Billinge, *J. Am. Chem. Soc.* **2013**, *135*, 6403.
- M. Risch, K. Klingan, F. Ringleb, P. Chernev, I. Zaharieva, A. Fischer, H. Dau, *ChemSusChem* **2012**, *5*, 542.
- D. González-Flores, I. Sánchez, I. Zaharieva, K. Klingan, J. Heidkamp, P. Chernev, P. W. Menezes, M. Driess, H. Dau, M. L. Montero, *Angew. Chem., Int. Ed.* **2015**, *54*, 2472.
- K. Klingan, F. Ringleb, I. Zaharieva, J. Heidkamp, P. Chernev, D. Gonzalez-Flores, M. Risch, A. Fischer, H. Dau, *ChemSusChem* **2014**, *7*, 1301.
- C. N. Brodsky, D. K. Bediako, C. Shi, T. P. Keane, C. Costentin, S. J. L. Billinge, D. G. Nocera, *ACS Appl. Energy Mater.* **2019**, *2*, 3.
- P. Rekha, S. Yadav, L. Singh, *Ceram. Int.* **2021**, *47*, 16385.
- S. Anantharaj, V. Aravindan, *Adv. Energy Mater.* **2020**, *10*, 1902666.
- K. Xu, H. Cheng, L. Liu, H. Lv, X. Wu, C. Wu, Y. Xie, *Nano Lett.* **2017**, *17*, 578.
- X. Ren, R. Ge, Y. Zhang, D. Liu, D. Wu, X. Sun, B. Du, Q. Wei, *J. Mater. Chem. A* **2017**, *5*, 7291.
- L. Yang, D. Liu, S. Hao, R. Kong, A. M. Asiri, C. Zhang, X. Sun, *J. Mater. Chem. A* **2017**, *5*, 7305.
- L. Xie, R. Zhang, L. Cui, D. Liu, S. Hao, Y. Ma, G. Du, A. M. Asiri, X. Sun, *Angew. Chem., Int. Ed.* **2017**, *56*, 1064.
- R. Q. Li, P. Hu, M. Miao, Y. Li, X. F. Jiang, Q. Wu, Z. Meng, Z. Hu, Y. Bando, X. B. Wang, *J. Mater. Chem. A* **2018**, *6*, 24767.
- C. Xie, Y. Wang, D. Yan, L. Tao, S. Wang, *Nanoscale* **2017**, *9*, 16059.
- H. Jiang, Q. He, X. Li, X. Su, Y. Zhang, S. Chen, S. Zhang, G. Zhang, J. Jiang, Y. Luo, P. M. Ajayan, L. Song, *Adv. Mater.* **2019**, *31*, 1805127.

- [22] D. Cao, D. Liu, S. Chen, O. A. Moses, X. Chen, W. Xu, C. Wu, L. Zheng, S. Chu, H. Jiang, C. Wang, B. Ge, X. Wu, J. Zhang, L. Song, *Energy Environ. Sci.* **2021**, *14*, 906.
- [23] J. N. Hausmann, S. Mebs, K. Laun, I. Zebger, H. Dau, P. W. Menezes, M. Driess, *Energy Environ. Sci.* **2020**, *13*, 3607.
- [24] J. Villalobos, D. González-Flores, R. Urcuyo, M. L. Montero, G. Schuck, P. Beyer, M. Risch, *Adv. Energy Mater.* **2021**, *11*, 2101737.
- [25] J. N. Hausmann, P. W. Menezes, *Angew. Chem., Int. Ed.* **2022**, *61*, e202207279.
- [26] P. W. Menezes, A. Indra, I. Zaharieva, C. Walter, S. Loos, S. Hoffmann, R. Schlögl, H. Dau, M. Driess, *Energy Environ. Sci.* **2019**, *12*, 988.
- [27] P. W. Menezes, C. Walter, B. Chakraborty, J. N. Hausmann, I. Zaharieva, A. Frick, E. Hauff, H. Dau, M. Driess, *Adv. Mater.* **2021**, *33*, 2004098.
- [28] J. Kwon, H. Han, S. Jo, S. Choi, K. Y. Chung, G. Ali, K. Park, U. Paik, T. Song, *Adv. Energy Mater.* **2021**, *11*, 2100624.
- [29] P. W. Menezes, S. Hoffmann, Y. Prots, W. Schnelle, R. Kniep, *Inorg. Chim. Acta* **2010**, *363*, 4299.
- [30] M. Risch, F. Ringleb, M. Kohlhoff, P. Bogdanoff, P. Chernev, I. Zaharieva, H. Dau, *Energy Environ. Sci.* **2015**, *8*, 661.
- [31] J. B. Gerken, E. C. Landis, R. J. Hamers, S. S. Stahl, *ChemSusChem* **2010**, *3*, 1176.
- [32] A. Indra, P. W. Menezes, I. Zaharieva, H. Dau, M. Driess, *J. Mater. Chem. A* **2020**, *8*, 2637.
- [33] Y. Surendranath, M. W. Kanan, D. G. Nocera, *J. Am. Chem. Soc.* **2010**, *132*, 16501.
- [34] J. B. Gerken, J. G. McAlpin, J. Y. C. Chen, M. L. Rigsby, W. H. Casey, R. D. Britt, S. S. Stahl, *J. Am. Chem. Soc.* **2011**, *133*, 14431.
- [35] J. Villalobos, D. González-Flores, K. Klingan, P. Chernev, P. Kubella, R. Urcuyo, C. Pasquini, M. R. Mohammadi, R. D. L. Smith, M. L. Montero, H. Dau, *Phys. Chem. Chem. Phys.* **2019**, *21*, 12485.
- [36] A. Bergmann, T. E. Jones, E. M. Moreno, D. Teschner, P. Chernev, M. Gliech, T. Reier, H. Dau, P. Strasser, *Nat. Catal.* **2018**, *1*, 711.
- [37] A. M. Ullman, C. N. Brodsky, N. Li, S. L. Zheng, D. G. Nocera, *J. Am. Chem. Soc.* **2016**, *138*, 4229.
- [38] J. T. Mefford, A. R. Akbashev, M. Kang, C. L. Bentley, W. E. Gent, H. D. Deng, D. H. Alsem, Y. Yu, N. J. Salmon, D. A. Shapiro, P. R. Unwin, W. C. Chueh, *Nature* **2021**, *593*, 67.
- [39] Y. Surendranath, D. A. Lutterman, Y. Liu, D. G. Nocera, *J. Am. Chem. Soc.* **2012**, *134*, 6326.
- [40] C. Pasquini, I. Zaharieva, D. González-Flores, P. Chernev, M. R. Mohammadi, L. Guidoni, R. D. L. Smith, H. Dau, *J. Am. Chem. Soc.* **2019**, *141*, 2938.
- [41] C. Costentin, T. R. Porter, J. M. Savéant, *J. Am. Chem. Soc.* **2016**, *138*, 5615.
- [42] H. Dau, C. Pasquini, *Inorganics* **2019**, *7*, 20.
- [43] T. Shinagawa, M. T. K. Ng, K. Takanabe, *ChemSusChem* **2017**, *10*, 4155.
- [44] T. Nishimoto, T. Shinagawa, T. Naito, K. Takanabe, *ChemSusChem* **2021**, *14*, 1554.
- [45] K. Obata, R. van de Krol, M. Schwarze, R. Schomäcker, F. F. Abdi, *Energy Environ. Sci.* **2020**, *13*, 5104.
- [46] A. J. Bard, L. R. Faulkner, *Electrochemical Methods: Fundamentals and Applications*, John Wiley & Sons, Inc, New York **2001**.
- [47] M. Plevová, J. Hnát, K. Bouzek, *J. Power Sources* **2021**, *507*, 230072.
- [48] T. Naito, T. Shinagawa, T. Nishimoto, K. Takanabe, *ChemSusChem* **2020**, *13*, 5921.
- [49] B. Zhang, Q. Daniel, M. Cheng, L. Fan, L. Sun, *Faraday Discuss.* **2017**, *198*, 169.
- [50] A. J. Esswein, Y. Surendranath, S. Y. Reece, D. G. Nocera, *Energy Environ. Sci.* **2011**, *4*, 499.
- [51] A. Peugeot, C. E. Creissen, D. Karapinar, H. N. Tran, M. Schreiber, M. Fontecave, *Joule* **2021**, *5*, 1281.
- [52] Z. Shi, X. Wang, J. Ge, C. Liu, W. Xing, *Nanoscale* **2020**, *12*, 13249.
- [53] J. N. Hausmann, R. Beltrán-Suito, S. Mebs, V. Hlukhyy, T. F. Fässler, H. Dau, M. Driess, P. W. Menezes, *Adv. Mater.* **2021**, *33*, 2008823.
- [54] J. N. Hausmann, B. Traynor, R. J. Myers, M. Driess, P. W. Menezes, *ACS Energy Lett.* **2021**, *6*, 3567.
- [55] M. R. Mohammadi, S. Loos, P. Chernev, C. Pasquini, I. Zaharieva, D. González-Flores, P. Kubella, K. Klingan, R. D. L. Smith, H. Dau, *ACS Catal.* **2020**, *10*, 7990.
- [56] M. W. Kanan, D. G. Nocera, *Science* **2008**, *321*, 1072.